Journal Pre-proofs

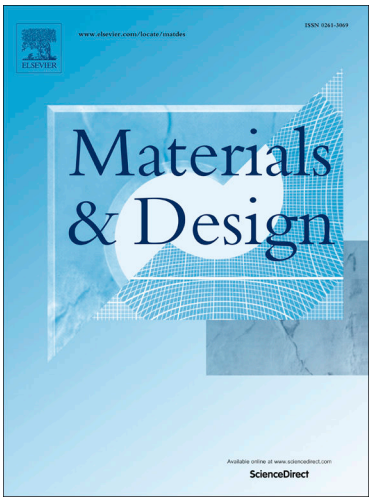


# Electric pulse improving the plasticity of the HAl66-6-3-2 alloy by promoting the formation of specific oriented texture

Bobo Lu, Kai Tang, Mingxia Wu, Yi Yang, Gang Yang

PII: S0264-1275(25)00256-4
DOI: https://doi.org/10.1016/j.matdes.2025.113836
Reference: JMADE 113836

To appear in: *Materials & Design*

Received Date: 7 November 2024
Revised Date: 8 March 2025
Accepted Date: 11 March 2025

Please cite this article as: Lu, B., Tang, K., Wu, M., Yang, Y., Yang, G., Electric pulse improving the plasticity of the HAl66-6-3-2 alloy by promoting the formation of specific oriented texture, *Materials & Design* (2025), doi: https://doi.org/10.1016/j.matdes.2025.113836

# Electric Pulse Improving the Plasticity of the HAl66-6-3-2 Alloy by Promoting the Formation of Specific Oriented Texture

*Bobo Lu, Kai Tang, Mingxia Wu, Yi Yang, Gang Yang**

School of Mechanical Engineering, Sichuan University, Chengdu 610065, China

E-mail address: yanggang66@sina.com (G. Yang).

**Abstract:** Electric pulse treatment (EPT) effectively enhances material plasticity but typically compromises strength, and the combined mechanisms of pulsed current on dislocation evolution and grain rotation remain unclear. Here, HAl66-6-3-2 alloy was subjected to EPT, and the results revealed that the EPT sample achieved an increase in plasticity without compromising the strength, with an elongation rate enhancement of 69.89%. The changes in performance are mainly attributed to three aspects: grain refinement, slight decrease in dislocation density, and the formation of strong {632} <223> texture during the EPT. Unlike the untreated (UT) samples with entangled dislocations, under the coupling effect of Joule heating and non-thermal effect, the dislocations in EPT samples exhibited directionality, primarily composed of a series of parallel dislocation pairs. The formation of the strong {632} <223> texture primarily relied on grain boundary migration and grain rotation, with both Joule heating and non-thermal effect facilitating rapid grain boundary migration. At low-angle grain boundaries, the pulsed current facilitated grain rotation, transforming low-angle grain boundaries in the $\beta$ phase into high-angle grain boundaries. The study demonstrates EPT can promote the movement of atoms and regulate the microstructure, which is of great significance for the subsequent control of alloy properties.

**Keywords:** electric pulse, parallel dislocations, grain refinement, grain rotation, grain boundary migration

## 1. Introduction

Electric pulse treatment (EPT), as a post-processing method, can significantly enhance the plasticity of materials and has attracted widespread attention due to its green and efficient characteristics[1, 2]. Many scholars have found that after electric pulse processing, the dislocation density of alloys decreases, which is conducive to improving the plasticity and fatigue performance of the alloy[3, 4]. The electroplasticity and thermal effects induced by pulsed current facilitate the motion of dislocations under an electric field by reducing the energy barrier for atomic diffusion[5-7], thereby eliminating dislocation tangles and

decreasing dislocation density. From a kinetic perspective, the non-thermal effects of pulsed current promote alterations in dislocation morphology[8-11], consequently accelerating the separation of dislocation tangles. Yan et al.[12] discovered that pulsed current facilitates dislocation motion and annihilation by reducing the activation energy, thereby decreasing the resistance to dislocation movement near pinning points. Xu et al.[13] found that in the process of electro-assisted stretching, the non-thermal effect of pulsed current is more likely to promote the movement of dislocations in copper metal.

To further clarify the specific mechanism of electric pulse, scholars have been dedicated to decoupling and analyzing the Joule heating and non-thermal effect in pulsed current. In recent years, Zhao et al.[14] made a simple distinction between Joule heating and electric pulses, demonstrating that compared to continuous currents, electric pulses can promote dislocation cross-slip, alter dislocation morphology, and form waves. Li et al.[15] confirmed through DFT (density functional theory) simulations and in-situ TEM (transmission electron microscopy) characterization that the electric field can reduce the sliding energy barrier to alter the sliding of charged dislocations. The mechanism of action of pulsed current primarily focuses on the study and discussion of dislocations. In fact, the effect of pulsed current on grain boundary migration, grain rotation, and grain orientation also significantly impacts the performance of alloys.

Pan et al.[16] found that EPT not only enhances [101]//ED texture but also promotes the migration of low-angle grain boundaries (LAGBs), thus achieving grain refinement. Kuang et al.[17] found that an anomalous texture was formed in magnesium alloys during the rolling process under the influence of electric pulses. Zhou et al.[18] discovered that compared to traditional heat annealing, pulsed current affects grain rotation, promotes grain boundary migration, and forms a strong {001}<010> texture. Rahman et al.[19] decoupled thermal effects from traditional electric pulse processes using in-situ EBSD (electron backscatter diffraction) technology at room temperature, observed that the grain rotation angle can reach up to 18° with changes in the direction of the pulsed current, and smaller grain sizes facilitate accelerated grain rotation. Waryoba et al.[20] decoupled Joule heating from pulsed current and found that non-thermal effect can promote grain rotation at LAGBs, proposing a grain rotation-induced grain growth mechanism. Currently, research on grain rotation and grain boundary migration under the influence of pulsed electric fields is limited, especially studies that discuss the combined effects of pulsed current on dislocation evolution and grain rotation are scarce.

Here, we conducted EPT and heat treatment (HT) on the HAl66-6-3-2 alloy, followed by tensile testing. Generally, pulsed current promotes dislocation glide to enhance plasticity often accompanied by a decrease in dislocation density. However, research results show that the strength of the specimens after EPT did not decrease, but plasticity significantly improved. It was found that under the action of pulsed current, the morphology and density of dislocations changed, forming a strong {632} <223> texture parallel to the current direction. The specimens were characterized using EBSD and TEM techniques, distinguishing the effects of pulsed current and heat effect on dislocation and grain orientation. In particular, the impact mechanisms of Joule heating and non-thermal effect on dislocations, grain boundary migration, and grain rotation were discussed. The understanding of the mechanisms of pulsed current on dislocation evolution and grain rotation is of significant importance for further control of alloy properties.

## 2. Experimental Section

### 2.1 Fabrication of Tensile Specimens

The HAl66-6-3-2 alloy was cut into non-standard tensile specimens using wire electrical discharge machining, with the dimensions of the tensile section being 8 mm in length, 2 mm in width and 1 mm in thickness. The tensile specimens were subjected to EPT and HT, and the surface temperature of the samples was monitored in real-time using a thermocouple, which recorded the temperature every 10 ms. The number of repeatability tests of the tensile curve under each parameter is 5 times. The frequency of the pulse current is 50 Hz, and the waveform is a square wave with a pulse width of 10 ms. Each cycle lasts for 1 s and is composed of 8 positive square waves and 8 negative square waves, with an interval of 680 ms between cycles. The number of repeatability tests of the tensile curve under each parameter is 5 times. The current density is defined as the ratio of the current to the cross-sectional area of the sample, with the current value being directly read from the EPT equipment. Furthermore, the strain rate for the tensile test is set at 2 mm $s^{-1}$. The technical parameters for each pulsed electric field and thermal treatment are shown in Table 1.

### 2.2 Characterization

The microstructure and chemical composition of the dog bone specimens were characterized by field-emission scanning electron microscopy (FESEM, Hitachi S-4800) equipped with an EDX analyzer, TEM (FEI Talos F200s) with selected area electron diffraction (SAED), and high-resolution transmission electron microscopy (HRTEM). The phase structures of samples were examined by using Micro-zone X-ray diffraction (XRD, Rigaku D/Max-2400) with Cu Kα radiation (λ=1.54 Å). The microstructure analysis was carried out by optical microscopy (OM) and EBSD and the observation area was located in the center of section of each sample. The step size of EBSD analysis was 0.32 μm. Fracture morphology was acquired from scanning electron microscopy (SEM, Phenom ProX).

**Table 1.** Technical parameters of pulsed electric field and thermal treatment

| Sample No. | Voltage (V) | Current density $j_e$ (A $mm^{-2}$) | Processing time (s) | Temperature (◦C) |
|---|---|---|---|---|
| UT | / | / | / | 29 |
| EPT-0 | 0.9 | 173 | 300 | 112 |
| EPT-1 | 1.0 | 190 | 300 | 156 |

| | | | | |
|---|---|---|---|---|
| EPT-2 | 1.1 | 203 | 300 | 189 |
| EPT-3 | 1.2 | 218 | 300 | 232 |
| EPT-4 | 1.3 | 231 | 300 | 261 |
| HT | / | / | 300 | 232 |

## 3. Results and Discussion

### 3.1 The Influence of Pulsed Current on Alloy Properties

As shown in Figure 1a-b, the untreated (UT) sample has a tensile strength of around 700 MPa and a total elongation of approximately 7.64%, indicating poor plasticity. During the EPT process, the plasticity of the alloy first increases and then decreases with the increase of current density, reaching the total elongation rate (12.98%) under the process condition EPT-3, with a significant increase of 69.89%. The decrease in total elongation rate under the EPT-4 treatment condition can be attributed to the high current density causing over-processing of the material. At elevated current densities, the Joule heating effect induces an excessively high temperature in the sample, leading to grain coarsening and a subsequent deterioration in material properties. Interestingly, under various EPT treatment conditions, the material's strength remains constant (approximately 707 MPa). Furthermore, in the HT experiment corresponding to EPT-3, the plasticity of the material is enhanced to some extent, with a total elongation of 9.39%, representing a 22.90% increase. However, there is a significant decrease in tensile strength (approximately 580 MPa), with a decrease rate of 17%. This indicates that the mechanisms of EPT and HT are not the same, and the mechanism of EPT cannot be simply attributed to the Joule heating effect. In Figure 1c, the temperature gradually increases due to the growing Joule heating caused by the increasing current density. During the EPT process, the relationship between temperature and current density mostly follows the law[21, 22]:

$$\Delta T = \frac{J^2}{C\mathrm{d}}(1)$$

here, $J$ represents the current density, $\rho$ is the electrical resistivity of the material, $\Delta t$ is the duration of the current application, and $C$ is the specific heat capacity of the material and $d$ is material density. In Figure 1d, the temperature shows an almost linear relationship with $J^2$, which is consistent with the law of temperature rise caused by pulsed current. In electrical plasticity, the Joule heating effect plays an annealing role, enhancing the plasticity of the alloy, but at the cost of reduced strength[23]. Considering that EPT-3 not only significantly improves plasticity but also maintains strength, to further clarify the influence mechanism of pulsed current, microstructural characterization was carried out on UT, EPT-3, and HT samples. (Subsequently mentioned EPT samples refer to the EPT-3 sample. All samples were characterized

in the post-treatment stage, prior to the onset of stretching.)

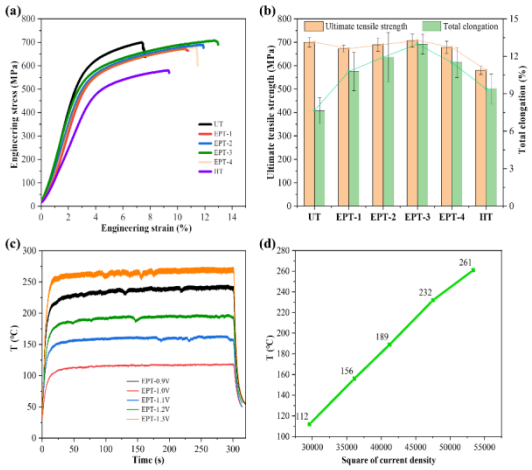


**Figure 1**. **a**) Tensile curves and **b**) comparison of ultimate tensile strength and elongation of the material under different treatment methods. **c**) Surface temperature of the specimens subjected to EPT. **d**) The relationship between temperature and the square of current density.

### 3.2 The Influence of Pulse Current on Grain Size

In Figure 2a-c, there is no significant change in the precipitate phase of the EPT sample, while the black precipitate phase in the HT sample has noticeably grown. In Figures 2d-f, in addition to the matrix microstructure, there are two types of precipitates: white (Pb phase) and black (Fe phase). The Fe precipitate phase is a hard phase that can enhance the strength of the sample but reduce its plasticity. The dispersed Fe precipitates in the UT sample can strengthen the sample, achieving a strength of up to 700 MPa. There is no significant change in the size of the precipitates after EPT, whereas after HT, the Fe precipitates have grown noticeably, which can reduce both the strength and plasticity of the sample. Due to thermal effects, secondary precipitation occurs on the surface of high-temperature samples, resulting in an increase in the size of the precipitated phase and a change in morphology. Compared with HT sample, there was no significant change in the precipitates in EPT samples. The interaction between electrons and atoms plays a crucial role in the pulse current, as localized high temperatures and reduced nucleation barriers lead to the dissolution of unstable phases[24], and the electric field and stress reduce the activation energy of stable phase precipitation[25, 26]. Furthermore, the application of electric pulsing enhances the aging diffusion coefficient, increases the nucleation rate, and decreases the critical nucleation radius of the second phase, resulting in relatively smaller precipitated phases[27]. Therefore, during the EPT period, dissolution and precipitation can be significantly accelerated[28], so that the precipitated phase does not grow significantly. As depicted in Figure 2g-i, phase changes after EPT are not pronounced, while the content of the $\gamma$-phase significantly increases after HT, which is consistent with the conclusions drawn in Figures 2a-c. As shown in Figure 2j, compared to the UT sample, the $\alpha$-phase grains in the EPT sample become smaller, while those in the HT sample enlarge. Similarly, in Figure 2l, the changes in the $\gamma$-phase grains in the EPT and HT samples are consistent with those of the $\alpha$-phase grains. In contrast, as shown in Figure 2k, the $\beta$-phase

grains in the EPT and HT samples decrease in size compared to the UT sample. This indicates that for the $\alpha$ and $\gamma$-phases, a phase transformation of $\alpha \rightarrow \gamma$ and grain coarsening occur during the HT process under the influence of heat[29]. Notably, In the EPT process, under the coupled effect of Joule heating and non-thermal effect, grain refinement is achieved within each phase[30], which is beneficial for enhancing the plasticity and strength of the samples.

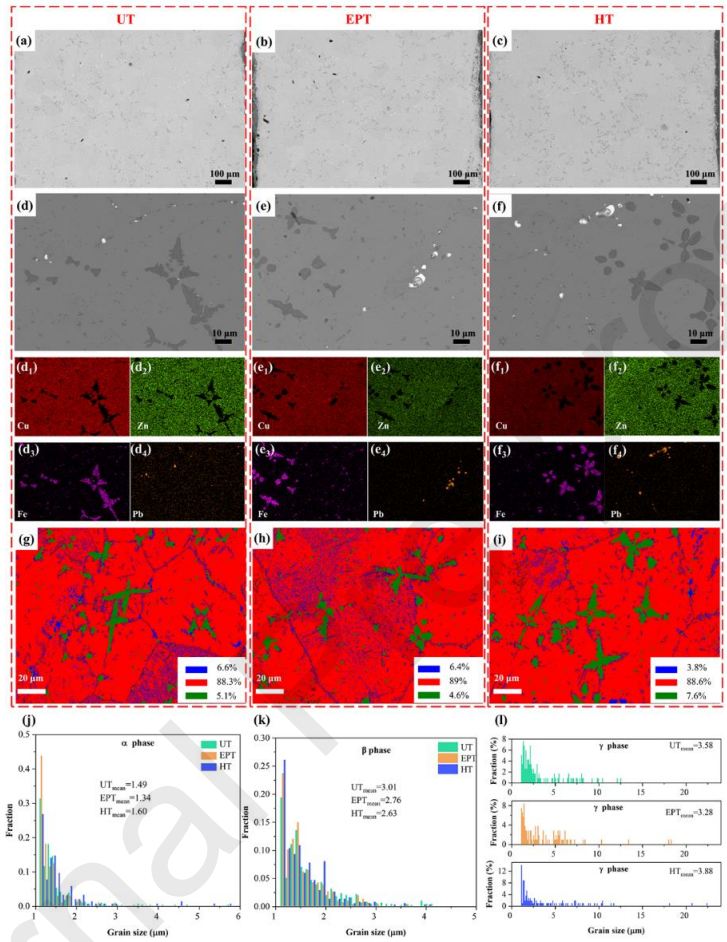


**Figure 2.** Low-magnification backscattered electron (BSE) images of **a**) UT sample, **b**) EPT sample, and **c**) HT sample. High-magnification BSE images of **d**) UT sample, **e**) EPT sample, and **f**) HT sample. **$d_1$-$d_4$**) Mapping images of Figure 2d. **$e_1$-$e_4$**) Mapping images of Figure 2e. **$f_1$-$f_4$**) Mapping images of Figure 2f. The phase distribution maps of **g**) UT sample, **h**) EPT sample, and **i**) HT sample (Blue represents $\alpha$-phase, red represents $\beta$-phase, and green represents phase $\gamma$-phase). The grain size distribution of **j**) $\alpha$-phase, **k**) $\beta$-phase, and **l**) $\gamma$-phase.

Figure 3a-c correspond to the EDS elemental mappings of Figure 2a-c. It can be observed that the content of elements does not change significantly after EPT and HT. Notably, the content of the Fe element in the sample slightly increases after HT, which is related to the limited range of EDS and the uneven distribution of Fe precipitates along the longitudinal direction, with noticeable growth of surface Fe precipitates. Additionally, as shown in Figure 3d, the UT sample is primarily composed of the $\beta$-phase

(CuZn PDF#00-002-1231) and $\alpha$-phase ($Cu_{0.64}Zn_{0.36}$ PDF#00-050-1333), with no significant phase changes observed in the EPT and HT samples. As is shown in Table 2, compared to the UT sample, the XRD peak widths at half maximum of the EPT and HT samples decrease[31], particularly for the HT sample, indicating a significant reduction in dislocation density due to dislocation annihilation under the influence of heat[32, 33].

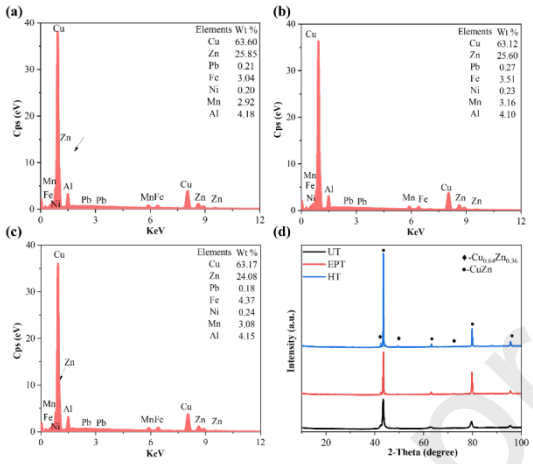


**Figure 3.** The energy dispersive spectroscopy (EDS) spectra of **a**) UT sample, **b**) EPT sample, and **c**) HT sample. **d**) XRD patterns of the UT, EPT, and HT samples.

**Table 2.** The FWHM values of the corresponding alpha and beta phases in Figure 3d

| | | | | | |
|---|---|---|---|---|---|
| | | ***β*-phase** | | | |
| UT | 2θ/° | 43.408 | 62.788 | 79.595 | 95.301 |
| | FWHM | 0.536 | 0.831 | 0.688 | 0.680 |
| EPT | 2θ/° | 43.507 | 63.154 | 79.751 | 95.537 |
| | FWHM | 0.250 | 0.333 | 0.261 | 0.453 |
| HT | 2θ/° | 43.437 | 63.180 | 79.801 | 95.511 |
| | FWHM | 0.153 | 0.278 | 0.197 | 0.342 |
| | | ***α*-phase** | | | |

| | | | | |
|---|---|---|---|---|
| UT | 2θ/° | 43.359 | 49.235 | 72.422 |
| | FWHM | 0.489 | 0.410 | 0.448 |
| EPT | 2θ/° | 42.434 | 49.446 | 72.402 |
| | FWHM | 0.216 | 0.335 | 0.384 |
| HT | 2θ/° | 42.435 | 49.345 | 72.432 |
| | FWHM | 0.187 | 0.321 | 0.383 |

### 3.3 The Effect of Pulsed Current on Texture

The distribution diagrams of grain boundaries and phase boundaries are shown in Figures 4a-c. The sample grains are mainly composed of numerous small grains and a few abnormal grains. The counted grain number is in the hundreds, which provides statistical significance for the analysis. As shown in Figure 4d-f, the IPF Coloring diagrams illustrate significant changes in grain orientation after EPT and HT treatments. Furthermore, compared to the UT and HT samples, the sample treated with pulsed current exhibited a pronounced preferred orientation, increasing the anisotropy of the alloy. As depicted in Figure 4g-i, in the UT sample, there the $\alpha$-phase mainly exist <101> // TD (transverse direction) fiber textures, the $\beta$-phase are mainly <112> // ND (normal direction) fiber textures and <102> // TD fiber textures and the $\gamma$-phase are mainly <100> // RD and <111> // RD fiber textures. The texture types and orientations of the samples after EPT and HT have changed, especially the EPT sample showing an overall increase in texture intensity, with the appearance of a <223> // RD (rolling direction) fiber texture, which is beneficial for the enhancement of strength and tensile plasticity in the EPT sample[34]. Compared to the UT sample, the fiber texture parallel to the RD direction increases after HT, such as <113> texture, indicates that the tensile plasticity of the sample after HT is improved.

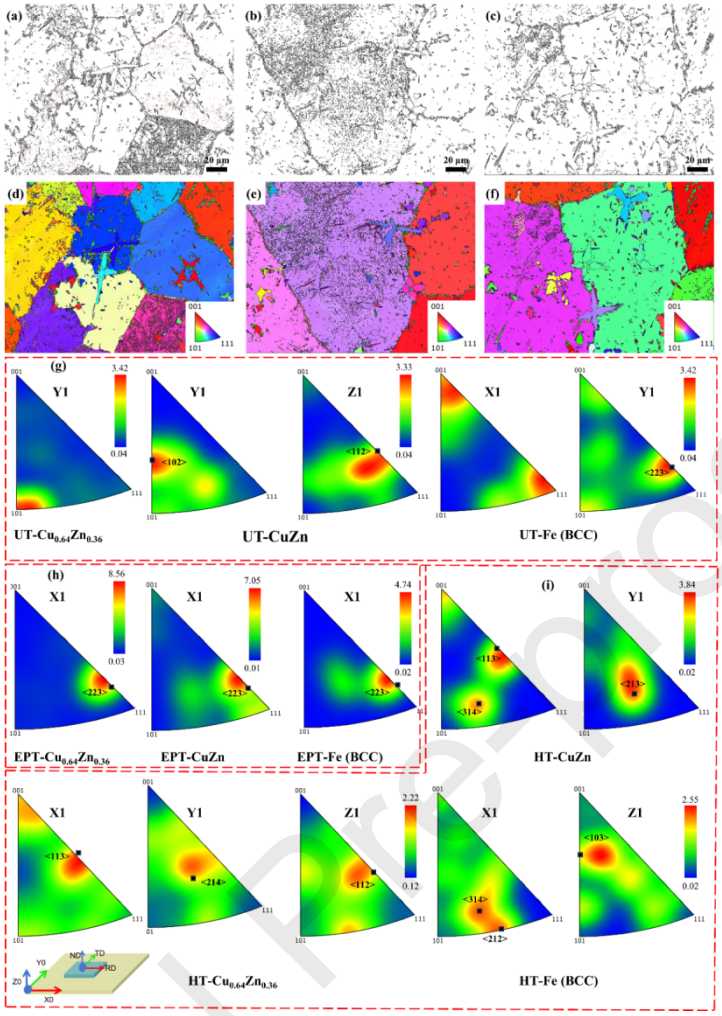


**Figure 4.** The distribution map of grain boundaries and phase boundaries of the **a**) UT, **b**) EPT, and **c**) HT samples (The red lines represent LAGBs, and the black lines represent HAGBs and phase boundaries). The Inverse Pole Figure (IPF) Coloring diagrams of the **d**) UT, **e**) EPT, and **f**) HT samples (the black lines represent HAGBs). IPF diagrams of the g) UT, h) EPT, and i) HT samples.

As depicted in Figure 5a-c, the $\alpha$-phase of the UT sample predominantly exhibits {121} <1$\bar{3}$1> texture, while the EPT sample's $\alpha$-phase primarily displays {632} <223> texture, and the HT sample's $\alpha$-phase mainly consists of {121} <1$\bar{3}\bar{1}$>, {301} <010>, and {123} <111>. Regarding the $\beta$-phase, the UT sample is characterized by {123} <111>, whereas the EPT and HT samples are distinguished by the presence of {632} <223> and {121} <1$\bar{3}\bar{1}$> planar textures, respectively. Additionally, in the $\gamma$-phase of the UT sample, the main textures are {123} <111> and {235} <502> plane textures, while in the samples after EPT and HT, the main textures are {632} <223> and {121} <131> plane textures, respectively. All samples also exhibit a pronounced $\gamma$-fiber texture (<010> // RD). The predominant texture types change after EPT and HT, indicating that grain rotation and orientation alterations occur under the influence of pulsed current[35] and heat[36]. Notably, contrary to previous studies suggesting that pulsed current reduces texture intensity

to enhance plasticity[37], the texture strength of each phase increases after EPT, primarily forming {632} <223> strong textures parallel to the RD, thereby enhancing the material's plasticity.

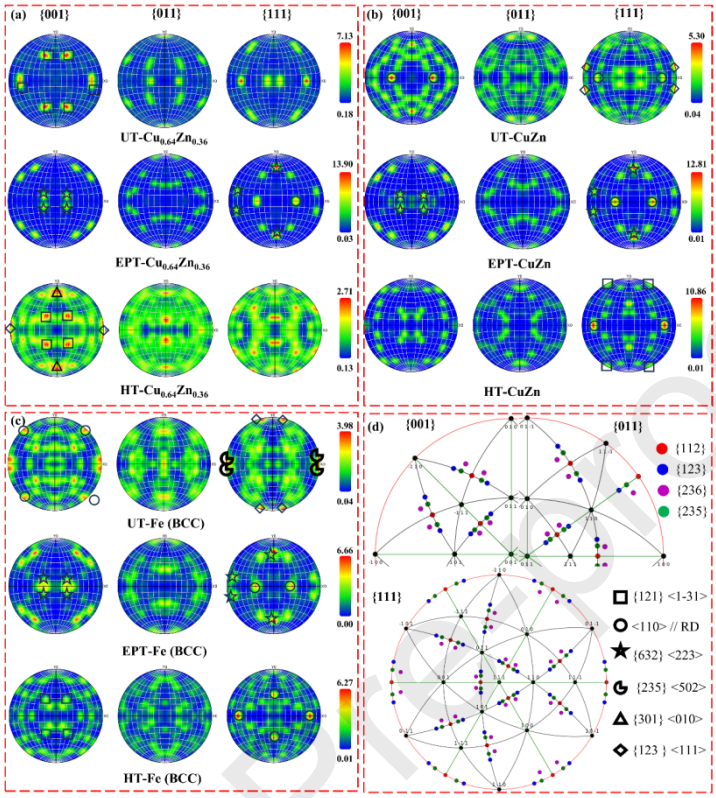


**Figure 5. a-c**) The pole figure (PF) of each material. **d**) The standard pole figures of {001}, {011}, and {111} crystal planes in a simple cubic structure.

### 3.4 The Impact of Pulsed Current on Dislocations

In Figure 6a-c, comparing with Figure 4d-f, it can be observed that the dislocation density distribution is orientation-dependent, being concentrated within specific oriented grains. Compared to the UT and EPT samples, the dislocation density in the HT sample is significantly reduced, which is consistent with the results of the XRD peak width changes. The quantitative analysis of dislocations obtained from the KAM maps is depicted in Figures 6d-l. Compared to the UT sample, the dislocation density in the EPT sample is slightly reduced, while in the HT sample, the dislocation density is nearly halved. It is evident that the HT sample exhibits reduced strength and enhanced plasticity.

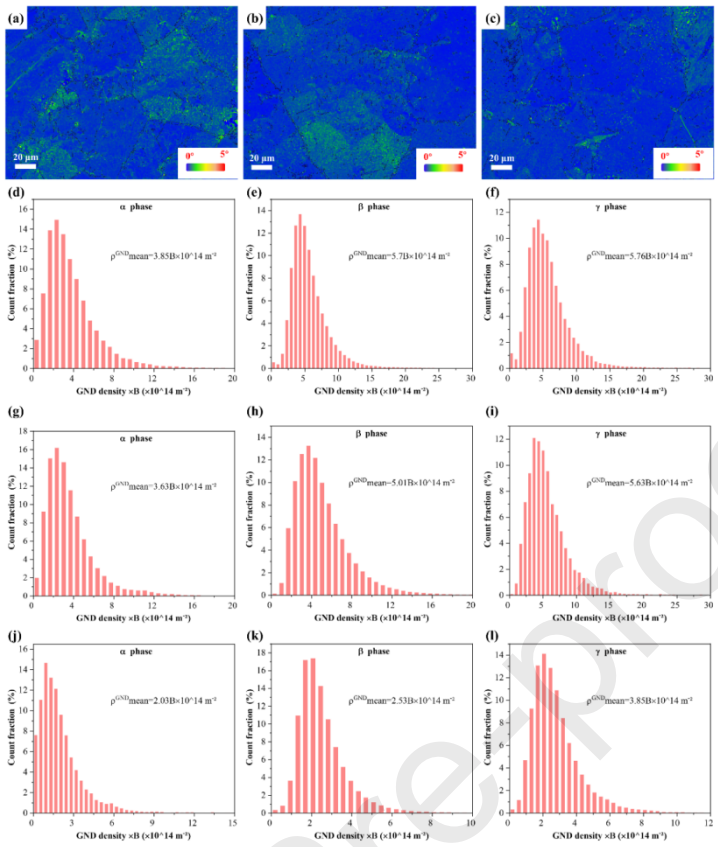


**Figure 6.** The Kernel average misorientation (KAM) maps of **a**) UT sample, **b**) EPT sample, and **c**) HT sample. **d-f**) Dislocation density distributions for the $\alpha$, $\beta$, and $\gamma$ phases of the UT sample, respectively (Figure 6d-f dislocation data are taken from Figure 6a). **g-i**) Dislocation density distributions for the $\alpha$, $\beta$, and $\gamma$ phases of the EPT sample, respectively (Figure 6g-i dislocation data are taken from Figure 6b). **j-l**) Dislocation density distributions for the $\alpha$, $\beta$, and $\gamma$ phases of the HT sample, respectively (Figure 6j-ldislocation data are taken from Figure 6c).

As shown in Figure 7a-b, the red arrows indicate that dislocations in the UT sample primarily exist in the form of dislocation walls and dislocation tangles. Figure 7c shows that matrix microstructure in Figure 7b is a single crystal CuZn ($\beta$-phase). As shown in Figure 7d, dislocations of EPT sample are primarily concentrated in the areas marked by the white dashed lines. In Figure 7e, parallel dislocations are observed, as indicated by red arrow-2, and red arrow-1 reveals some stacking fault. Similarly, some parallel dislocations can also be observed in Figure 7f, g. The inset in Figure 7f indicates that the grains on both sides of the grain boundary are $\beta$-phase. Figure 7h is the grain boundary area marked by the red arrow in Figure 7f, showing that the two sides of the grain boundary are the {110} planes of the $\beta$-phase. Figure 7i, enlarging the red box area of 7h, reveals that atoms of different orientations have formed {110} stacking fault structures. However, in Figure 7j, the dislocation density after HT is significantly reduced, and the precipitation of Fe is clearly observable. Figure 7k is the area indicated by the red line frame in Figure 7j, where stacking faults can be seen aggregated at the grain boundaries, and dislocations are dispersed

throughout the grain interior. Figure 7l is the area indicated by the red arrow in Figure 7j, showing the grains on both sides of the grain boundary to be differently oriented planes. The lattice spacing in regions 1 and 2 is d = 0.22 nm corresponding to the $\alpha$ phase {111} planes. Compared to the UT sample, the EPT sample exhibited specifically oriented parallel dislocations, while the density of dislocations in the HT sample significantly decreased with dislocations predominantly manifesting as pinned dislocations. This observation suggests that the evolution mechanisms of dislocations under Joule heating and pulsed current is different.

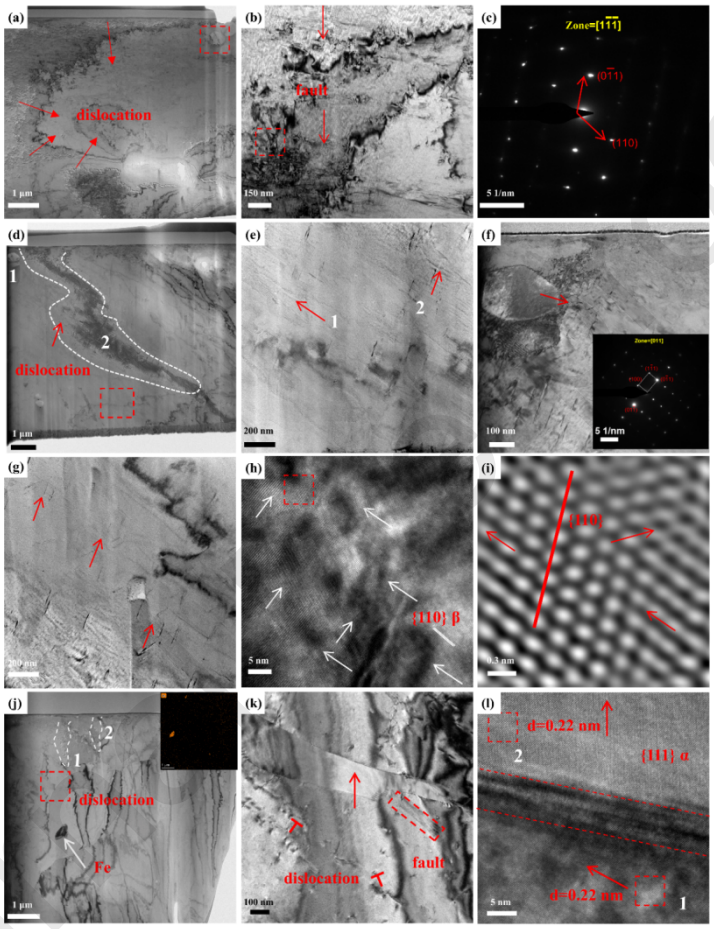


**Figure 7.** Microstructural characterization of (a-c) UT sample, (d-i) EPT sample, (g-i) HT sample. **a**) Low-magnification TEM image. **b**) High-magnification TEM image. **c**) SAED pattern corresponding to Figure 7b. **d**) Low-magnification TEM image. **e**) Magnified image of the red dashed box in Figure 7d. **f**) Enlarged image of the area marked '1' in Figure 7d, with the inset showing the corresponding SAED pattern. **g**) Low-magnification TEM image. **h**) HRTEM image of the area marked by the '2' arrow in Figure 7e. **i**) Enlarged image of the area enclosed by the red dashed line in Figure 7h. **j)** Low-magnification TEM image, with the inset showing the elemental mapping distribution of Fe. **k)** Magnified image of the red dashed box in Figure 7j. **l)** HRTEM image of the area marked by the arrow in Figure 7k.

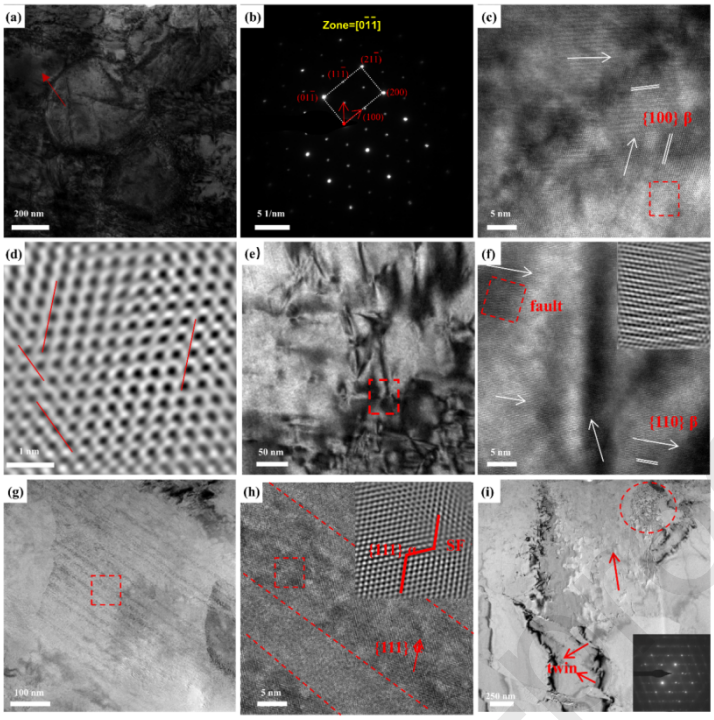


**Figure 8.** Microstructural characterization of **(a-f)** HT sample, **(g-h)** EPT sample, **(l)** HT sample. **a**) Enlarged image of the red dashed box in Figure 7a. **b**) SAED pattern corresponding to Figure 8a. **c**) High-resolution image of the region marked by the red arrow in Figure 8a. **d**) Enlarged image of the red dashed box in Figure 8d. **e**) Enlarged image of the red dashed box in Figure 7b. **f**) High-resolution image of the region marked by the red dashed box in Figure 8e, with the inset showing an enlarged the red dashed box. **g**) Enlarged image of the area marked by the '1' arrow in Figure 7e. **h**) HRTEM image enclosed by the red dashed line in Figure 8g, with the inset showing an enlarged view of the red dashed line box. **i**) e) Enlarged image of the area marked '1' in Figure 7j, with the inset showing the corresponding SAED image.

In Figure 8a-d, many defects aggregate at the grain boundaries and the grains on both sides of the grain boundary are $\beta$-phase in UT sample. Notably, in Figure 8b, some stacking fault structures of the {100} planes can be observed[38]. Figure 8c illustrates that the microstructures on either side of the grain boundary exhibit different orientations of the {100} planes. Figure 8d shows coherent distortions of stacking fault at the {100} crystal planes, which is consistent with the result in Figure 8b. Figure 8e is the part enclosed by the red line frame in Figure 7b, showing some dislocation tangles within the grain interior. As shown in Figure 8f, the lattice distortion at the dislocation entanglement sites is particularly pronounced. In Figure 8g, h. EPT sample exhibits some {111} stacking fault structures (SFs) of $\alpha$-phase. In Figure 8i, there are some twin structures and dislocation tangles in HT sample. It is evident that the dislocation entanglements of UT sample are opened after EPT and HT, which is beneficial for enhancing the plasticity of the samples.

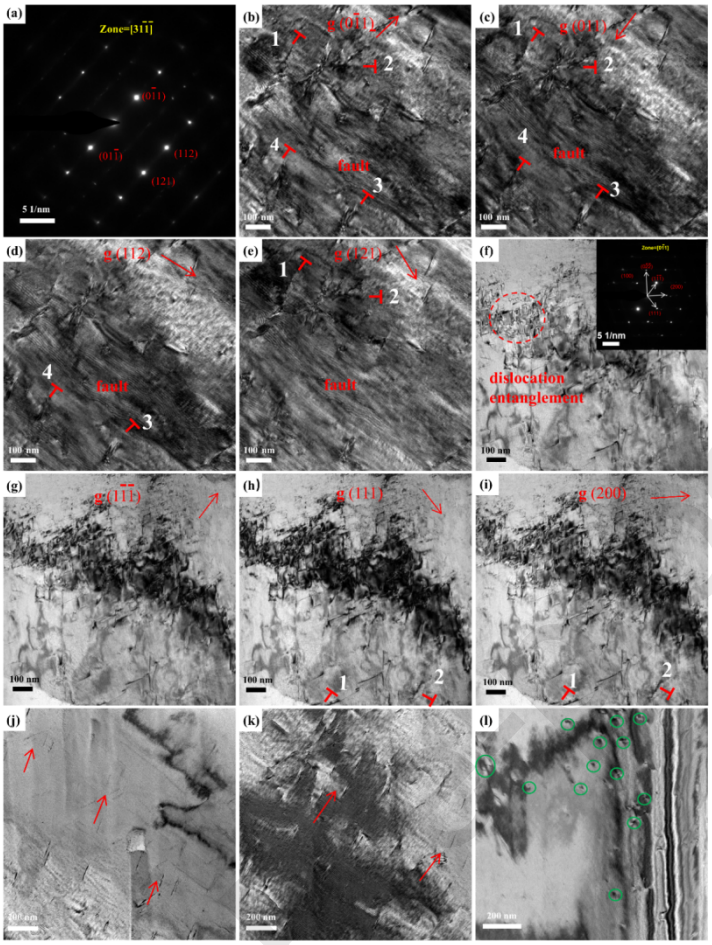


**Figure 9.** Microstructural characterization of (**a-e**) EPT sample, (**f-i**) HT sample. **a**) SAED pattern of the area marked '2' in Figure 7d. **b-e**) Bright-field images taken under the [3$\bar{1}\bar{1}$] zone axis with different *g*-vectors. **f**) Enlarged image of the area marked '2' in Figure 7j, with the inset showing the corresponding SAED image. **g-i**) Bright-field images taken under the [0$\bar{1}$1] zone axis with different *g*-vectors. **g, h**) TEM images of EPT sample of different regions. **l**) TEM images of HT sample of different regions.

Imaging using different spots of EPT sample from Figure 9a is shown in Figures 9b-e. A comparison shows that dislocation 1 is an edge dislocation with Burgers vector $b = \pm 1/2[11\bar{1}]$, dislocation 2 is a mixed dislocation with $b = \pm 1/2[11\bar{1}]$, and dislocations 3 and 4 are mixed dislocations with $b = \pm 1/2[1\bar{1}1]$. In Figure 9f-i, clear dislocation tangles can also be observed in HT sample. A comparison reveals that dislocation 1 is a mixed dislocation with Burgers vector $b = \pm 1/2[110]$, and dislocation 2 is a helical dislocation with $b = \pm 1/2[110]$. The dislocations after EPT are mainly edge dislocations and mixed dislocations, while the dislocations after HT are primarily screw dislocations and mixed dislocations. Notably, the dislocation entanglements are nearly completely resolved after EPT, whereas some entanglements remain after HT, which is consistent with previously observed phenomena. In Figures 9j-l, the changes in dislocation configurations after EPT and HT are different. In comparison to the UT samples, which exhibit dislocation tangling, the EPT samples mainly show parallel dislocations, while the HT

samples predominantly feature partially tangled dislocations and dislocation loops. Compared to the changes in dislocation types, the variations in dislocation configurations are of greater significance, as they facilitate a deeper understanding of dislocation evolution under pulsed electric current.

In summary, the HT sample shows dislocation annihilation under the influence of heat, with a significant reduction in dislocation density. In addition, the twin structure of $\alpha$-phase is also conducive to the improvement of the plasticity of the sample. In contrast, the entanglement dislocation of the EPT sample is opened and exhibited parallel edge dislocations and mixed dislocations. During EPT process, the movement of dislocations is promoted under synergistic effects of thermal and non-thermal, resulting in parallel dislocations[39] and SFs[40, 41].

## 4. Discussion

### 4.1 Evolution of Dislocations under Pulsed Current

Research indicates that pulsed current significantly enhances dislocation mobility, thereby facilitating the unlocking of tangled dislocations[42]. The widely accepted view among scholars is as follows: 1) The Joule heating effect can promote atomic and dislocation motion, thereby facilitating the activation of slip systems[43]; 2) The "local hotspots" formed by distortion scattering[44] also contribute to the unlocking of tangled dislocations[45]; 3) Under high-density currents ($10^{\wedge 5\text{-}6}$ A mm$^{-2}$), the Electron wind effect can facilitate dislocation rearrangement and slip, leading to the unlocking of tangled dislocations[46] and inducing the regeneration of partial dislocations[47, 48]. However, based on the current density at the level of $10^{\wedge 2}$ A mm$^{-2}$ in this study, the effects of the electron wind alone can be neglected. Similarly, the magnetic effects can also be neglected[49, 50].

Regarding the evolution of dislocations under pulsed current, Li et al.[51] established a dislocation model based on thermal and non-thermal effects from a kinetic perspective. They proposed that during the pulsed current treatment process, the thermal effect primarily promotes the thermally activated motion of dislocations, while the non-thermal effect weakens the interaction between dislocations and defects, accelerating dislocation velocity and even altering the dislocation slip mechanism. Lian et al.[52] suggested that the coupling of thermal and non-thermal effects of pulsed current promotes the formation of specifically oriented parallel dislocations around precipitated phases. Zhou et al.[53] validated through in-situ TEM techniques that at a current density of 26.5 A mm$^{-2}$, the Electron wind effect facilitates the thermally activated unlocking of screw dislocations, resulting in the formation of linear dislocations.

In general, when the slip direction is $[uvw]$, the shear stress $\tau$ and Burgers vector $b$ are as follows:

$$\tau \propto G \cdot b = G \cdot \frac{a}{n(u^2 + v^2 + w^2)^{\frac{1}{2}}} (2)$$

in the equation, $G$ represents the shear modulus, $a$ represents the lattice constant, and $n$ represents the type of dislocation (which can be perfect dislocations or partial dislocations, with $n$ being greater for partial dislocations than perfect dislocations). From equation (2), it can be observed that the shear stress $\tau$ is

inversely proportional to $n$, indicating that under the same conditions, the critical resolved shear stress of partial dislocations is lower than that of perfect dislocations.

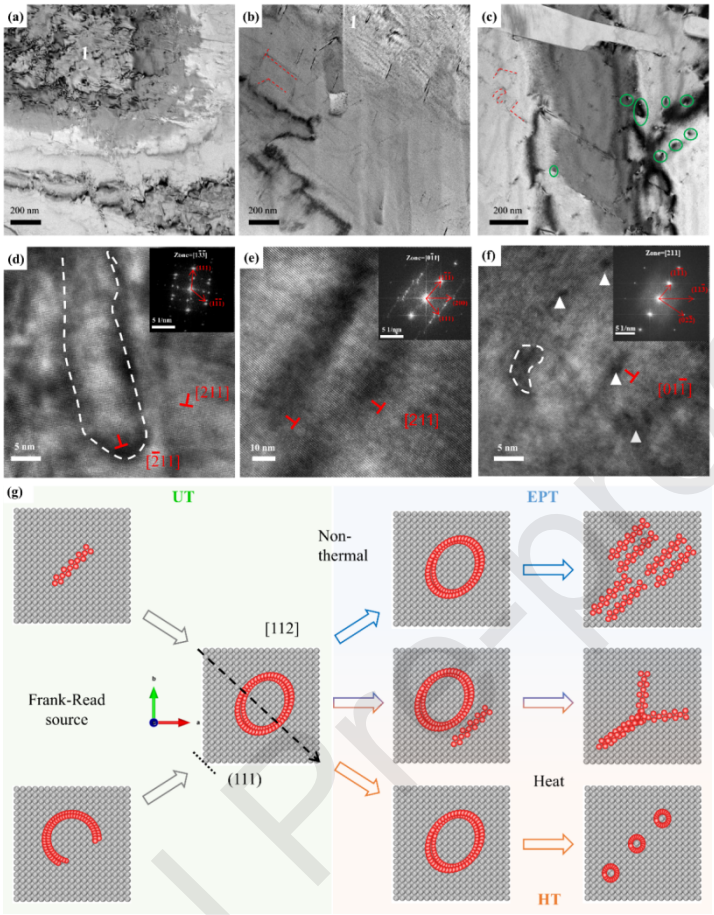


**Figure 10.** The TEM images of **a**) UT sample, **b**) EPT sample, and **c**) HT sample. The high-resolution images of **d**) UT sample (The illustration is the corresponding SAED image), **e**) EPT sample (The illustration is the corresponding SAED image), and **f**) HT sample (The illustration is the corresponding SAED image), **g**) Schematic diagram of dislocation evolution.

As shown in Figure 10a, dislocations in the UT sample predominantly exist in the form of dislocation tangles. 'Bow-shaped' dislocations and 'linear' dislocations can be observed at the position marked by 1. From the SAED in Figure 10d, e, spots with obvious fault characteristics can be observed. In Figure 10d, the UT sample contains dislocation loops, with one end of the loop consisting of Shockley dislocations 1/6[211] and 1/6[211]. In Figure 10b, e, after EPT, dislocations mainly exist as parallel dislocation pairs and the parallel dislocations are primarily Shockley dislocations 1/6[211]. In contrast, Figure 10c, f depicts the dislocation in HT sample, which is mainly composed of dislocation loops of 1/2[01$\bar{1}$]. As illustrated in Figure 10g, under pulsed current, the coupled effect of Joule heating and non-thermal effect accelerates the movement of dislocations, which annihilate while also proliferating through the Frank-Read source mechanism. During the pulsed current process, Frank-Read sources first form dislocation loops, and under the action of the non-thermal effect, dislocations at both ends of the loops annihilate, with the splitting at

the ends of the loops forming parallel dislocation. The dislocation annihilation is marked by red dashed lines in Figure 10b, c. Under the influence of heat, dislocation loops encountering moving dislocation lines undergo interaction when the loop plane is perpendicular to the glide plane of the dislocation line, causing the dislocation loop to flip. The flipped dislocation loop makes contact with the dislocation line and annihilates at the intersection[54]. Li et al.[55] used molecular dynamics (MD) and in situ TEM observations to demonstrate that the encounter between the dislocation loop plane and the dislocation line can cause dislocation annihilation. As shown by the green loop in Figure 10c, another annihilation mechanism exists under the influence of heat, where metastable larger dislocation loops expand and annihilate in the free direction, forming concentric pinned dislocation loops[56].

The annihilation dislocation reactions are shown as follows:

$$\frac{1}{6}[\bar{2}11] + \frac{1}{6}[2\bar{1}\bar{1}] \rightarrow 0 \quad (3)$$

**4.2 Evolution of Texture under Pulsed Current**

As shown in Figure 11a-c, compared to the UT sample, both EPT and HT result in preferred orientations of different textures. In Figure 11d-f, the *α*-phase of the UT sample is primarily composed of two textures, {121} <1$\bar{3}$1> and <110>//RD, with area percentages of 32.5% and 27.7%, respectively. The [110] crystallographic direction is a high-density direction in the *α*-phase (FCC) crystal structure, characterized by lower surface energy, and typically possesses higher plasticity, being more prone to plastic deformation[57]. After EPT, the *α*-phase is mainly composed of two textures, {632} <223> and <110>//RD, with area percentages of 63.8% and 15.7%, respectively. The pulsed current reduced the proportion of <110>//RD, primarily because the direction of the pulsed current is aligned with the RD, preferentially acting on grains with the [110] orientation, causing grain rotation and leading to more plastic deformation. The *α*-phase after HT is mainly composed of textures <110>//RD, S ({123} <63$\bar{4}$>), {121} <1$\bar{3}$1>, and {130} <010>, with area percentages of 20.7%, 17.3%, 16.3%, and 12.5%, respectively. During the HT process, the proportion of {121} <1$\bar{3}$1> decreases, while the proportions of S ({123} <63$\bar{4}$>) and {130} <010> increase. It is noteworthy that in the EPT sample, the texture {632} <223> in the *α*-phase overlays the S ({123} <63$\bar{4}$>) texture, and it can be inferred that the evolution path of the texture in the EPT *α* phase is from {121} <1$\bar{3}$1> and <110>//RD to {123} <63$\bar{4}$>, and then to {632} <223>.

In Figure 11g-i, the *β*-phase of the UT sample is primarily composed of three textures, {123} <111>, <110>//RD, and {235} <502>, with area percentages of 31.1%, 32.5%, and 27.7%, respectively. After EPT, the *β*-phase is mainly composed of two textures, {632} <223> and {010} <2$\bar{1}$0>, with area percentages of 51.6% and 29.1%, respectively. After HT, the *β*-phase is primarily composed of two textures, <110>//RD and {121} <1$\bar{3}$1>, with area percentages of 47.8% and 35.3%, respectively. Comparing with the UT sample, it can be observed that during the HT process, the {123} <111> texture transforms into the {123} <1$\bar{3}$1> texture. The proportion of the <110>//RD texture type increases after HT. For the BCC phase, the <110> direction may have a higher atomic diffusion rate, thus being more likely to form and grow during the heat treatment process. It is noteworthy that in the EPT sample, the *β*-phase {0$\bar{1}$2} <142> overlays the

<110>//RD texture. Therefore, it can be inferred that the evolution path of the texture in the $\beta$-phase is {123} <111> → {123}<63$\bar{4}$> → {632} <223>, and <110>//RD → {010} <2$\bar{1}$0>.

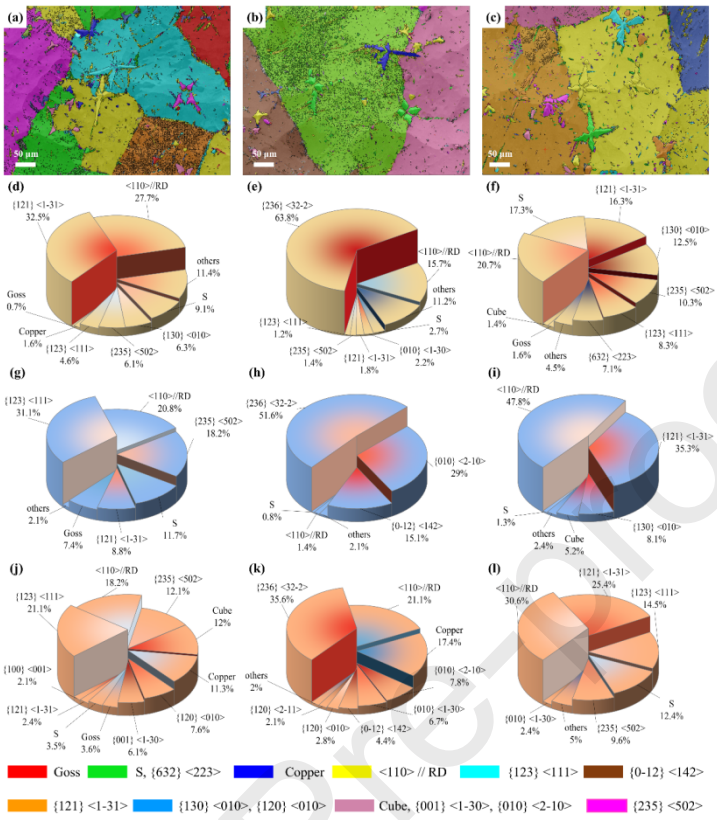


**Figure 11.** Texture distribution maps of **a**) UT sample, **b**) EPT sample, and **c**) HT sample. The $\alpha$-phase texture distribution of **d**) UT sample, **e**) EPT sample, and **f**) HT sample. The $\beta$-phase texture distribution of **g**) UT sample, **h**) EPT sample, and **i**) HT sample. The $\gamma$-phase texture distribution of **j**) UT sample, **k**) EPT sample, and **l**) HT sample.

In Figure 11j-l, the $\gamma$-phase of the UT sample is primarily composed of four textures: {123} <111>, <110>//RD, {235} <502>, and Cube ({001} <100>), with area percentages of 21.1%, 18.2%, 12.1%, and 12%, respectively. After EPT, the $\beta$-phase is mainly composed of two textures: {632} <223> and <110>//RD, with area percentages of 35.6% and 21.1%, respectively. After HT, the $\gamma$-phase is primarily composed of two textures: <110>//RD and {121} <1$\bar{3}$1>, with area percentages of 30.6% and 25.4%, respectively. Comparing the UT and EPT samples, it can be observed that during the HT process, the Copper texture ({112} <111>) and Cube ({100} <100>) transform into <110>//RD and {123} <1$\bar{3}$1> textures. It should be noted that after EPT and HT, the original Cube cubic texture disappears, which may be due to precipitation of the $\gamma$-phase. Therefore, it can be inferred that the evolution path of the texture in the $\gamma$-phase during the EPT process is {123} <111> → {123} <63$\bar{4}$> → {632} <223>.

Under the influence of pulsed current, grain-oriented rotation occurred, resulting in the formation of a specific {632} <223> texture. Similarly, Li et al.[58] also found that under the action of electric pulses, CuCrZr alloy preferentially forms the {112} <011> and {112} <110> texture, and the grain is also refined

with the change of texture orientation. Furthermore, Zhao et al.[59] also found that pulsed current can reduce dislocation density and promote grain rotation Guan et al.[60], and the severity of grain rotation increases with the increase of peak current density. It is evident that the formation of the {632} <223> texture is dependent on the pulsed current.

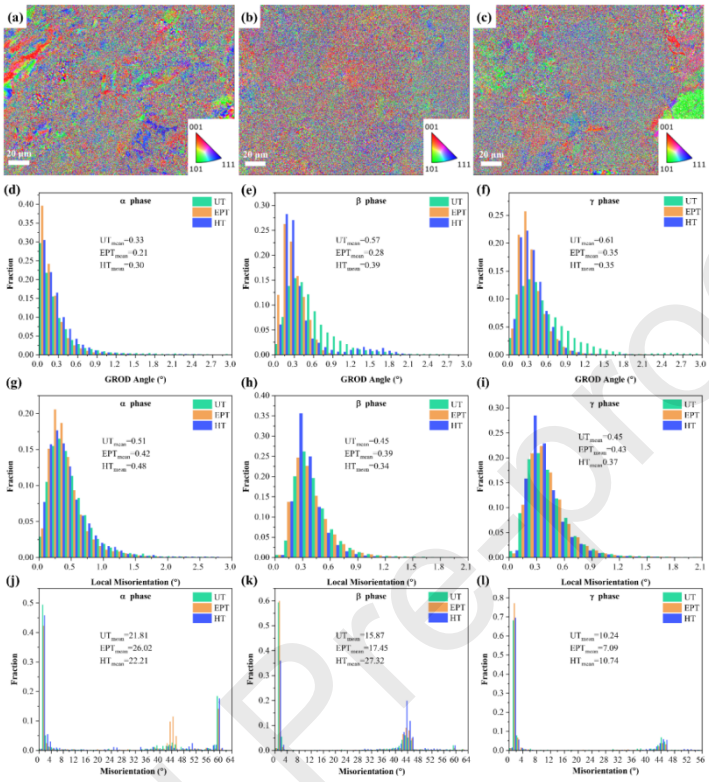


**Figure 12.** The Grain Reference Orientation Deviation (GROD) axis diagrams of **a**) UT sample, **b**) EPT sample, and **c**) HT sample. The GROD angle distributions of UT, EPT, and HT samples for **d**) $\alpha$-phase, **e**) $\beta$-phase, and **f**) $\gamma$-phase. Local Misorientation distributions of UT, EPT, and HT samples for **g**) $\alpha$-phase, **h**) $\beta$-phase, and **i**) $\gamma$-phase. Misorientation distributions of UT, EPT, and HT samples for **j**) $\alpha$-phase, **k**) $\beta$-phase, and **l**) $\gamma$-phase.

In Figure 12a-c, there is a partial but distinct preferential orientation of [001], [110], and [111] in the UT sample, while HT sample exhibits a pronounced preferential orientation of [110]. Compared to UT and HT samples, the absence of a pronounced texture orientation after EPT is attributed to the formation of atypical {632} <223> texture under pulsed current. In Figure 12d-f, compared to the UT sample, both HT and EPT samples show a decrease in GROD angle, mainly due to the increased proportion of texture components, which is consistent with Figure 11, especially Figure 11e, h, where the proportion of {632} <223> texture exceeds 50%. Furthermore, the texture intensity of the grains is enhanced after EPT (Figure 4, 5), which also contributes to the reduction in GROD angle. In Figure 12g-i, compared to the UT sample, both HT and EPT samples exhibit a decrease in local misorientation. For the EPT sample, the EPT process causes the grain orientation to tend to be uniform, resulting in a decrease in local misorientation. For the HT sample, in addition to the concentration of texture orientation, the decrease in local misorientation is

also attributed to the engulfment of surrounding subgrains or defects during grain growth[61], leading to a significant reduction in dislocation density (Figure 6j-l). In Figure 13j-l, an increase in misorientation can be observed after EPT and HT in the $\alpha$ and $\beta$-phases, while in the $\gamma$-phase, misorientation decreases after EPT but increases after HT. Due to grain growth, the grain size increases after HT, and grain growth occurs, leading to an increase in misorientation (Figure 2j). Similarly, misorientation increases in the $\gamma$-phase after HT. Although the overall grain size decreases after EPT and HT (Figure 2k), there are local overheating areas that cause some grains to grow[62], thereby increasing the misorientation between grains, which is consistent with the observations in Figure 2g-i. The grain size of the $\gamma$ phase decreases after EPT, and there are no abnormally grown areas (Figure 2l), leading to a decrease in misorientation with the reduction of grain size. The grain size of the $\alpha$ phase decreases after EPT, and there is no obvious abnormal growth. However, it can be observed that the $\alpha$ phase has a directional aggregation in distribution, and after EPT, the grain boundaries migrate towards the [223] direction (Figures 2g, h), resulting in an increase in the orientation difference between grains, thereby increasing misorientation. In summary, the migration of grain boundaries leads to grain refinement.

### 4.3 Pulsed Current Promotes Grain Boundary Migration and Grain Rotation

Based on the Arrhenius theory[63] of thermally activated processes. it is assumed that grain boundary migration is a thermally activated process, where atoms or molecules need to overcome a certain energy barrier $Q$ to migrate. The Arrhenius formula for the grain boundary migration rate is shown as follows[64]:

$M = M_0 exp\left(-\frac{Q}{kT}\right)$(4) the equation, $M$ represents the grain boundary migration rate, the pre-exponential factor $M_0$ contains information related to the atomic vibration frequency and the net atomic flux during each activation event, $k$ is the Boltzmann constant, and $T$ is the absolute temperature. Compared to the UT sample, the temperature $T$ increases after HT and EPT, especially in EPT where the atoms at the grain boundaries have a higher $T$, which is conducive to grain migration. Under pulsed current, compared to the UT and HT samples, the non-thermal effect can promote atomic migration, particularly near the grain boundaries. The non-thermal effect can increase the net atomic flux, thereby increasing $M_0$, and further accelerating the migration of grain boundaries.

The modified expression for the grain boundary migration rate is as follows:

$M = M_0^{'} exp\left(-\frac{Q^{'}}{kT^{'}}\right)$(5)here, $M_0^{'}$ is the modified pre-exponential factor, which takes into account the effects of Joule heating and the non-thermal effect, $Q^{'}$ is the modified activation energy, which may be reduced due to higher temperatures, and $T^{'}$ is the modified temperature, considering the temperature increase caused by Joule heating.

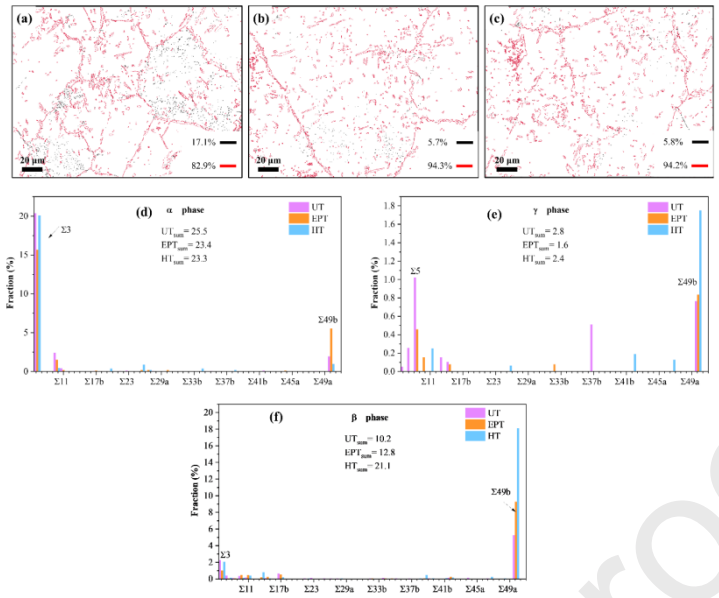


**Figure 13.** Grain boundary distribution maps of **a**) UT sample, **b**) EPT sample, and **c**) HT sample (black lines indicate low-angle grain boundaries, red lines indicate high-angle grain boundaries). Coincidence site lattice (CSL) grain boundary distributions for the UT, EPT, and HT samples in the **d**) $\alpha$-phase, **e**) $\gamma$-phase, and **f**) $\beta$-phase.

In Figure 13a-c, compared to the UT sample, the proportion of high-angle grain boundaries (HAGBs) increases in the EPT and HT samples, indicating that grain boundary migration occurred during the EPT and HT processes, achieving a transition from LAGBs to HAGBs. The increased proportion of HAGBs also helps to promote an increase in orientation differences between grains. In Figure 13d-f, compared to the UT samples, the samples after EPT exhibit an increase in the proportion of high-energy grain boundaries, consistent with the conclusion of an increase in the proportion of HAGBs. However, the proportion of special grain boundaries in the $\gamma$ phase after EPT decreases overall, indicating that the increased HAGBs after EPT are mainly the $\alpha$ and grain $\beta$ boundaries. On the other hand, in the HT sample, the proportion of the special grain boundaries shifts towards high-energy grain boundaries in the $\beta$ and $\gamma$ phases. Especially in the $\beta$-phase, the proportion of high-energy grain boundaries greatly increases, indicating that the increased HAGBs are mainly $\beta$-phase grain boundaries, which is consistent with the result of a significant increase in misorientation in Figure 12k. It is worth noting that in the $\alpha$-phase, the proportion of Σ3 does not change much after HT, indicating that some deformed twin boundaries in the UT sample have transformed into annealed twin boundaries.

A grain rotation rate model based on Fick's law, which derives the dependence of grain rotation rate on grain size under high pressure and temperature by adjusting the vacancy flux. The specific expression is as follows[65]:

$\frac{d\theta}{dt} = \frac{8\delta\,\Omega P}{f(Ln)} D_0 exp\left(-\frac{q}{kT}\right)$(6) the equation, $d\theta/dt$ represents the grain rotation rate, $\delta$ is the diffusion width

of the boundary, $\Omega$ is the atomic volume, $q$ is the activation energy, $f$ is a function of the grain size $L$, $n$ is a constant (ranging between 1 and 6), $D_0$ is the diffusion constant, $T$ and $P$ are the temperature and pressure. Grain rotation occurs at the grain boundary, and the rotation rate can be expressed as[66, 67]:

$$\frac{d\theta_{ij}}{dt} = \frac{8\Omega\delta_i P}{L_{ij}^2} D_0 exp\left(-\frac{q}{kT}\right) \quad (7)$$

here, $\theta_{ij}$ is the grain boundary misorientation between grain i and j, and $L_{ij}^2$ is the length of the grain boundary segment. $\delta_i$ is grain boundary thickness.

Under pulsed current, Joule heating and the non-thermal effect accelerate atomic motion, thereby increasing $D_0$. The non-thermal effect also increases $P$, and furthermore, the grain refinement caused by the pulsed current reduces $L_{ij}^2$. Compared to the HT sample, the EPT sample exhibits a higher grain rotation speed.

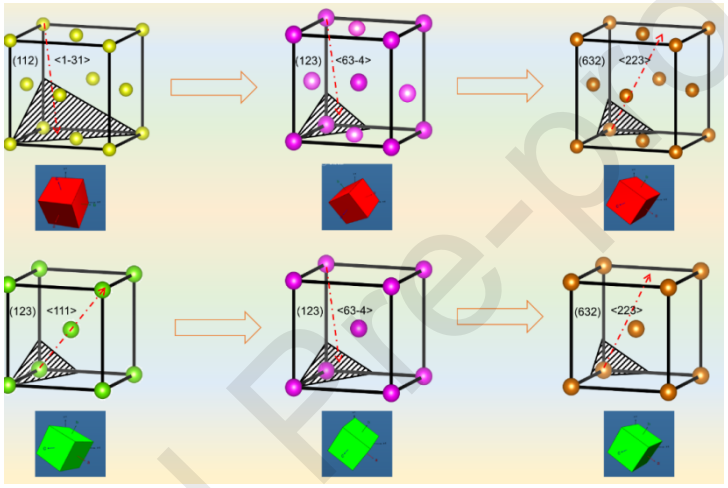


**Figure 14.** Diagram of grain rotation under pulsed current.

Regarding the effect of pulse current on grain rotation, in recent years, Waryoba et al.[68], through MD (Molecular Dynamics) simulation, found that pulsed current can promote the rotation of grain volume, achieving a grain growth mechanism. Zhang et al.[69] also discovered that the non-thermal effect of pulsed current facilitates the motion of dislocations at the grain boundaries, resulting in grain boundary slip and ultimately leading to grain rotation. As shown in Figure 14, during the EPT process, the coupling effect of Joule heating and the non-thermal effect causes changes in grain orientation, and the grain volume also rotates as the grain boundaries migrate. Grains oriented along [1$\bar{3}$1] and [111] rotate to the [223] orientation.

### 4.4 The Relationship between Texture and Plasticity under Pulsed Current

Since the tensile direction of the samples is the RD direction, the discussion of the Schmidt factor is based on the RD direction. As shown in Figure 15a-c, compared to the UT and HT samples, overall, The EPT sample contains a large number of readily deformable grains due to the elimination of grain that

difficult to slide, exhibiting favorable plastic behavior. The distribution and proportion of different slip systems on individual grains are shown in Figure 15d-f. In the $\alpha$-phase, the UT sample mainly exhibits {121} <1$\bar{3}$1> and {112} <1$\bar{1}$0> slip, the EPT mainly shows {632} <223> slip, while the HT sample primarily has {235} <502> and {121} <1$\bar{3}$1> slip systems. In the $\beta$ phase, UT, EPT, and HT samples exhibit multiple closely spaced slip systems. In the $\gamma$-phase, the UT sample mainly shows {123} <11$\bar{1}$> and {112} <1$\bar{1}$0> slip, the EPT mainly exhibits {010} <2$\bar{1}$0> slip, and the HT mainly activates {121} <1$\bar{3}$1>, {111} <1$\bar{1}$0>, and {112} <1$\bar{1}$0> slip systems. Compared to Figure 11a-c, the slip systems initiated in the $\alpha$-phase are mainly texture-controlled slip systems, which are conducive to increased plasticity. However, the $\beta$ phase, similar to the $\gamma$ phase, the initiation of grain slip occurs in slip systems different from those dominated by texture, which is not only related to the different orientations of the grains but also related to the internal defects of the grains, especially the $\beta$-phase of the EPT, where grains with {632} <223> texture have many grain boundaries and second phases inside, and their activated slip systems tend to be {0$\bar{1}$2} <142>. The comparison of the Schmidt factor in the same slip system on different grains for different phases is shown in Figure 15g-i. In the $\alpha$, $\beta$, and $\gamma$-phases, the Schmidt factor values for the texture-controlled slip systems are the highest for the UT, EPT, and HT samples, which are conducive to plastic deformation of the samples. However, for the EPT sample, the proportion of {632} <223> texture is much higher than others, and in different grains, the Schmidt factor of the {632} <223> slip system is relatively high, indicating a certain degree of plastic coordination between grains. This coordination helps to transfer stress between grains, reduce stress concentration at grain boundaries, and thereby enhance the overall plasticity of the material.

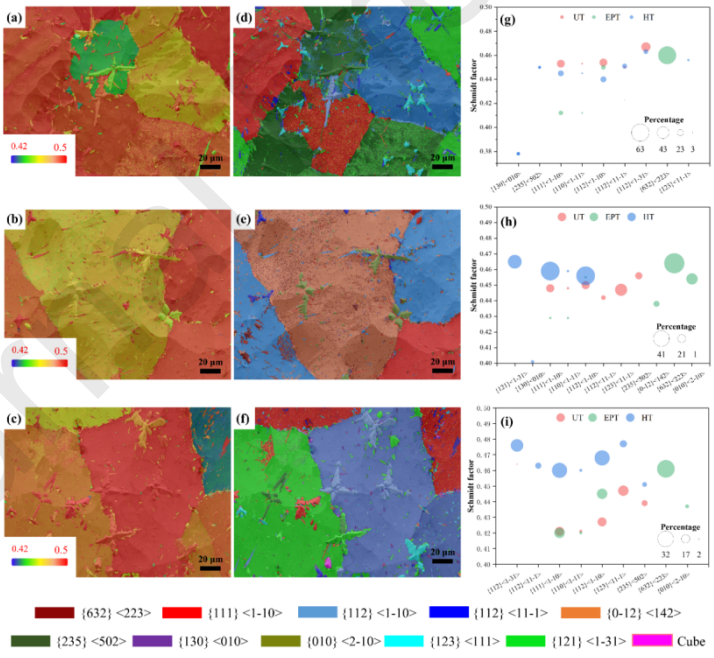


**Figure 15.** Schmidt factor diagrams of **a**) UT sample, **b**) EPT sample, and **c**) HT sample. Distribution maps of activated slip systems on individual grains for **d**) UT sample, **e**) EPT sample, and **f**) HT sample. Overall Schmidt factor distributions of the UT, EPT, and HT samples for **g**) $\alpha$-phase, **h**) $\beta$-phase, and **i**) $\gamma$-phase.

## 5. Conclusions

Here, the tensile tests of HAl66-6-3-2 alloys at UT, EPT and HT were compared. Compared to the UT sample, it was observed that under a pulsed current density of 218 A $mm^{-2}$, the tensile elongation was increased by 69.89% without reducing the strength. The evolution of dislocations and textures in UT, EPT, and HT samples was studied, revealing the mechanisms of texture formation and grain refinement induced by grain boundary migration and grain rotation.

(1) Compared to the UT sample, the dislocation density in the EPT sample is slightly reduced, while the dislocation density in the HT sample is significantly decreased. During the EPT process, the non-thermal effect promotes the multiplication of dislocations and the entanglement dislocation of the EPT sample is opened and exhibited parallel dislocations. Under the influence of heat, dislocation loops not only annihilate by interacting with dislocation lines but also undergo self-annihilation through repeated expansion in the direction of freedom.

(2) Under pulsed current, a strong {632} <223> texture is formed, and among different grains, the Schmidt factor of the {632} <223> slip system is relatively high, indicating a certain degree of plastic coordination between grains. This is conducive to stress transfer between grains, reduction of stress concentration at grain boundaries, and thereby enhances the overall plasticity of the material.

(3) By comparing with the UT sample, the pathway for the formation of the {632} <223> texture parallel to the current direction in the EPT sample is established: in the $\alpha$-phase: {121} <1$\bar{3}$1> → {123} <63$\bar{4}$> → {632} <223>. In the $\beta$ and $\gamma$-phases: {123} <111> → {123} <63$\bar{4}$> → {632} <223>.

(4) The formation of the strong {632} <223> texture primarily depends on grain boundary migration and grain rotation, with both Joule heating and the non-thermal effect contributing to the accelerated movement of grain boundaries. At LAGBs, the synergistic effects of thermal and non-thermal of pulsed current facilitates the motion grain boundary slip and grain rotation, transforming LAGBs into HAGBs in the $\beta$-phase.

(5) The migration of grain boundaries in the EPT sample also promotes grain refinement, while the HT sample engulfs a large number of dislocations during the grain boundary migration process. Compared to the UT sample, both the EPT and HT samples exhibit increased tensile elongation, but the strength of the EPT sample does not decrease.

## CRediT authorship contribution statement

**Bobo Lu:** Investigation, Data curation, Formal analysis, Writing – original draft, Writing – review & editing. **Kai Tang:** Writing – review & editing, Methodology. **Mingxia Wu:** Writing – review & editing, Validation, Resources. **Yi Yang**: Supervision. **Gang Yang:** Supervision, Resources.

## Data availability

Data will be made available on request.

## Acknowledgement

This work was supported by the National Natural Science Foundation of China (No.52375457) and the National Natural Science Foundation of China (Grant No. 52205490).

## References

[1] Yang Y, Qin R, Dong Y, Wang J, Ye C, Crystal plasticity modeling of electropulsing induced plasticity in metals, Int. J. Plasticity 171 (2023). https://doi.org/10.1016/j.ijplas.2023.103828.

[2] Li H, Peng LF, Meng B, Xu ZT, Wang LL, Ngaile G, et al., Energy field assisted metal forming: Current status, challenges and prospects, Int. J. Mach. Tools Manuf. 192 (2023) 104075. https://doi.org/10.1016/j.ijmachtools.2023.104075.

[3] Zhang S, Geng M, Kim MJ, Bae J-H, Nam Han H, Hong S-T, Prolonged fatigue life in aluminum clad steel by electropulsing treatment: Retardation of interface-microcrack formation, International Journal of Fatigue 167 (2023) 107376. https://doi.org/10.1016/j.ijfatigue.2022.107376.

[4] Roh J-H, Seo J-J, Hong S-T, Kim M-J, Han HN, Roth JT, The mechanical behavior of 5052-H32 aluminum alloys under a pulsed electric current, Int. J. Plasticity 58 (2014) 84-99. https://doi.org/10.1016/j.ijplas.2014.02.002.

[5] Yan J, Zhao R, Wan M, Meng B, Coupled effect of pulsed current and ultrasonic vibration on deformation behavior of Inconel 718 sheet: phenomena and modeling, J. Mater. Res. Technol. 25 (2023) 5538-5560. https://doi.org/10.1016/j.jmrt.2023.07.001.

[6] Sun P, Qu S, Duan C, Hu X, Li X, Improving the high cycle fatigue property of Ti6Al4V ELI alloy by optimizing the surface integrity through electric pulse combined with ultrasonic surface rolling process, J. Mater. Sci. Technol. 170 (2024) 103-121. https://doi.org/10.1016/j.jmst.2023.06.029.

[7] Xu G, Zhu Y, Peng L, Mi X, Xie H, Cao Y, et al., Simultaneously enhancing the strength and ductility of Cu-Ti-Fe alloy through electric current pulse induced precipitation, Scr. Mater. 255 (2025) 116387. https://doi.org/10.1016/j.scriptamat.2024.116387.

[8] Yu X, Gu S, Wang G, Kimura Y, Ju Y, Toku Y, Unveiling Thermal and Athermal Effects in Strain Hardening Removal of A6061 Aluminum Alloy, Met. Mater. Int. (2024). https://doi.org/10.1007/s12540-024-01778-7.

[9] Yu S, Xu K, Wang T, Xu Y, Luo S, Zhan L, et al., Effect of pulse current density on creep ageing behavior of 2195 Al-Li alloy, Mater. Sci. Eng., A 909 (2024) 146814. https://doi.org/10.1016/j.msea.2024.146814.

[10] Kim M-J, Bui-Thi T-A, Kang S-G, Hong S-T, Nam Han H, Electric current-induced phenomena in metallic materials, Current Opinion in Solid State and Materials Science 32 (2024) 101190. https://doi.org/10.1016/j.cossms.2024.101190.

[11] Xue L, Jiang J, Yang Y, Xu G, Liao C, Liu J, et al., An eco-friendly electric pulse treatment process for improving the microstructure and properties of cold-rolled pure copper sheet, Mater. Res. Express 10 (2023) 066513. https://doi.org/10.1088/2053-1591/ace02d.

[12] Yan J, Zhao R, He W, Wan M, Meng B, Mechanical behavior and underlying mechanism of nickel-based superalloy during coupling electrical pulse and

ultrasonic treatment, Mater. Sci. Eng., A 911 (2024) 146876. https://doi.org/10.1016/j.msea.2024.146876.

[13] Xu Z, Jiang T, Huang J, Peng L, Lai X, Fu MW, Electroplasticity in electrically-assisted forming: Process phenomena, performances and modelling, Int. J. Mach. Tools Manuf. 175 (2022) 103871. https://doi.org/10.1016/j.ijmachtools.2022.103871.

[14] Zhao S, Zhang R, Chong Y, Li X, Abu-Odeh A, Rothchild E, et al., Defect reconfiguration in a Ti-Al alloy via electroplasticity, Nat. Mater. 20 (2021) 468-472. https://doi.org/10.1038/s41563-020-00817-z.

[15] Li M, Shen Y, Luo K, An Q, Gao P, Xiao P, et al., Harnessing dislocation motion using an electric field, Nat. Mater. 22 (2023) 958-963. https://doi.org/10.1038/s41563-023-01572-7.

[16] Pan D, Wang Y, Guo Q, Zhang D, Xu X, Zhao Y, Grain refinement of Al–Mg–Si alloy without any mechanical deformation and matrix phase transformation via cyclic electro-pulsing treatment, Mater. Sci. Eng., A 807 (2021) 140916. https://doi.org/10.1016/j.msea.2021.140916.

[17] Kuang J, Low TSE, Niezgoda SR, Li X, Geng Y, Luo AA, et al., Abnormal texture development in magnesium alloy Mg-3Al-1Zn during large strain electroplastic rolling: Effect of pulsed electric current, Int. J. Plasticity 87 (2016) 86-99. https://doi.org/10.1016/j.ijplas.2016.09.004.

[18] Zhou M, Zhang X, Regulating the recrystallized grain to induce strong cube texture in oriented silicon steel, J. Mater. Sci. Technol. 96 (2022) 126-139. https://doi.org/10.1016/j.jmst.2021.03.081.

[19] Rahman MH, Oh H, Waryoba D, Haque A, Room temperature control of grain orientation via directionally modulated current pulses, Mater. Res. Express 10 (2023). https://doi.org/10.1088/2053-1591/ad0b56.

[20] Waryoba D, Islam Z, Wang B, Haque A, Recrystallization mechanisms of Zircaloy-4 alloy annealed by electric current, J. Alloys Compd. 820 (2020) 153409. https://doi.org/10.1016/j.jallcom.2019.153409.

[21] Sprecher AF, Mannan SL, Conrad H, Overview no. 49: On the mechanisms for the electroplastic effect in metals, Acta Metall. 34 (1986) 1145-1162. https://doi.org/10.1016/0001-6160(86)90001-5.

[22] Xiang S, Zhang X, Dislocation structure evolution under electroplastic effect, Mater. Sci. Eng., A 761 (2019) 138026. https://doi.org/10.1016/j.msea.2019.138026.

[23] Liu J, Jia D, Fu Y, Kong X, Lv Z, Zeng E, et al., Electroplasticity effects: from mechanism to application, Int. J. Adv. Manuf. Technol. 131 (2023) 3267-3286. https://doi.org/10.1007/s00170-023-12072-y.

[24] Jiang Y, Tang G, Shek C, Zhu Y, Xu Z, On the thermodynamics and kinetics of electropulsing induced dissolution of $\beta$-Mg17Al12 phase in an aged Mg-9Al-1Zn alloy, Acta Mater. 57 (2009) 4797-4808. https://doi.org/10.1016/j.actamat.2009.06.044.

[25] Liu W, Cui JZ, Effect of the homogenization treatment in an electric field on $T_1$ precipitation in 2091 Al-Li alloy, Scr. Metall. Mater. 33 (1995) 623-626. https://doi.org/10.1016/0956-716X(95)00267-Y.

[26] Chen K-X, Yan L-Z, Zhang Y-A, Li X-W, Li Z-H, Gao G-J, et al., Enhanced formability of Al–Mg–Si–Zn alloy sheet via dislocation structure and texture during cold rolling, J. Mater. Res. Technol. 28 (2024) 3306-3318. https://doi.org/10.1016/j.jmrt.2023.12.246.

[27] Shi D, Yu W, Gao G, Kang K. Effect of Electro-Pulse on Microstructure of Al-Cu-Mn-Zr-V Alloy during Aging Treatment and Mechanism Analysis. Metals2024. p. 648.

[28] Xu X, Zhao Y, Ma B, Zhang M, Rapid precipitation of T-phase in the 2024 aluminum alloy via cyclic electropulsing treatment, J. Alloys Compd. 610 (2014) 506-510. https://doi.org/10.1016/j.jallcom.2014.05.063.

[29] Sakai T, Dynamic recrystallization microstructures under hot working conditions, J. Mater. Process. Technol. 53 (1995) 349-361. https://doi.org/10.1016/0924-0136(95)01992-N.

[30] Xia Q, Chen C, Xiao G, Chen K, Zhou H, A modified dislocation density-based model of 30CrMnSiA considering the coupling effect of electroplasticity and grain refinement during the pulsed current-assisted plane strain deformation, J. Mater. Sci. 58 (2023) 12793-12810. https://doi.org/10.1007/s10853-023-08792-x.

[31] Das Bakshi S, Sinha D, Ghosh Chowdhury S, Anisotropic broadening of XRD peaks of α′-Fe: Williamson-Hall and Warren-Averbach analysis using full width at half maximum (FWHM) and integral breadth (IB), Mater. Charact. 142 (2018) 144-153. https://doi.org/10.1016/j.matchar.2018.05.018.

[32] He K, Chen N, Wang C, Wei L, Chen J, Method for Determining Crystal Grain Size by X-Ray Diffraction, Cryst. Res. Technol. 53 (2018) 1700157. https://doi.org/10.1002/crat.201700157.

[33] Renzetti RA, Sandim HRZ, Bolmaro RE, Suzuki PA, Möslang A, X-ray evaluation of dislocation density in ODS-Eurofer steel, Mater. Sci. Eng., A 534 (2012) 142-146. https://doi.org/10.1016/j.msea.2011.11.051.

[34] Wang C, Ning H, Liu S, You J, Wang T, Jia H-J, et al., Enhanced ductility and strength of Mg-1Zn-1Sn-0.3Y-0.2Ca alloy achieved by novel micro-texture design, Scr. Mater. 204 (2021) 114119. https://doi.org/10.1016/j.scriptamat.2021.114119.

[35] Zhang X, Li H, Shao G, Gao J, Zhan M, "Target effect" of pulsed current on the texture evolution behaviour of Ni-based superalloy during electrically-assisted tension, J. Alloys Compd. 898 (2022) 162762. https://doi.org/10.1016/j.jallcom.2021.162762.

[36] Takajo S, Merriman CC, Vogel SC, Field DP, In-situ EBSD study on the cube texture evolution in 3 wt% Si steel complemented by ex-situ EBSD experiment — From nucleation to grain growth, Acta Mater. 166 (2019) 100-112. https://doi.org/10.1016/j.actamat.2018.11.054.

[37] Fan W, Ren Z, Wei S, Liu Q, Wang T, Wu G, Effect of high energy electric pulse on microstructure and mechanical properties of pre-deformed SUS 304 ultra-thin strip, Mater. Sci. Eng., A 893 (2024). https://doi.org/10.1016/j.msea.2023.145364.

[38] Li X, Zhao Q, Tian Y, Wang Q, Fan J, Song K, et al., Phase transformation induced transitional twin boundary in body-centered cubic metals, Acta Mater. 249 (2023). https://doi.org/10.1016/j.actamat.2023.118815.

[39] Xiao A, Huang C, Liu H, Cui X, Wang S, Deformation Mechanism of 5052 Aluminum Alloy Using Electrically Assisted Electromagnetic Forming, Met. Mater. Int. 28 (2022) 2483-2497. https://doi.org/10.1007/s12540-021-01130-3.

[40] Yue X, Hu S, Yin F, Hua L, Athermally induced MC carbide decomposition in gradient M50 bearing steels during electric pulse treatments, J. Mater. Sci. 58 (2023) 15251-15263. https://doi.org/10.1007/s10853-023-08985-4.

[41] Geng B, Liu Z, Li Y, Wang G, Zhou R, Analysis of evolution law and mechanism of stacking fault density of M7C3 carbides under the action of the electric current pulse, Mater. Charact. 191 (2022) 112117. https://doi.org/10.1016/j.matchar.2022.112117.

[42] Fan Y, Fan H, Hao Z, Effect of pulsed current on plastic deformation of Inconel 718 under high strain rate and high temperature conditions, J. Alloys Compd. 943 (2023) 169150. https://doi.org/10.1016/j.jallcom.2023.169150.

[43] Li M, Zhang B, Chen G, Li X, Zhang X, Li H, Temperature dependence of electroplastic effect on reducing the ultimate stress in Ti-6Al-2Zr-1Mo-1V alloy during tension, Mater. Sci. Eng., A 863 (2023) 144545. https://doi.org/10.1016/j.msea.2022.144545.

[44] Rudolf C, Goswami R, Kang W, Thomas J, Effects of electric current on the plastic deformation behavior of pure copper, iron, and titanium, Acta Mater. 209 (2021) 116776. https://doi.org/10.1016/j.actamat.2021.116776.

[45] Yang Z, Bao J, Ding C, Son S, Ning Z, Xu J, et al., Electroplasticity in the Al0.6CoCrFeNiMn high entropy alloy subjected to electrically-assisted uniaxial tension, J. Mater. Sci. Technol. 148 (2023) 209-221. https://doi.org/10.1016/j.jmst.2022.11.031.

[46] Zhang H, Wang X, Ma Y, Gu X, Lu J, Wang K, et al., Formability and mechanism of pulsed current pretreatment–assisted laser impact microforming, Int. J. Adv. Manuf. Technol. 114 (2021) 1011-1029. https://doi.org/10.1007/s00170-021-06964-0.

[47] Liang C-L, Lin K-L, The amorphous interphase formed in an intermetallic-free Cu/Sn couple during early stage electromigration, Scr. Mater. 155 (2018) 58-62. https://doi.org/10.1016/j.scriptamat.2018.06.024.

[48] Liao Y-H, Chen C-H, Liang C-L, Lin K-L, Wu AT, A comprehensive study of electromigration in pure Sn: Effects on crystallinity, microstructure, and electrical property, Acta Mater. 200 (2020) 200-210. https://doi.org/10.1016/j.actamat.2020.09.010.

[49] Jeong K, Jin S-W, Kang S-G, Park J-W, Jeong H-J, Hong S-T, et al., Athermally enhanced recrystallization kinetics of ultra-low carbon steel via electric current treatment, Acta Mater. 232 (2022) 117925. https://doi.org/10.1016/j.actamat.2022.117925.

[50] Lin S, Chu X, Feng D, Zhao Z, Gao J, Electric pulse-induced suppression of the Portevin – Le Chatelier behavior of 5086 aluminum alloy under uniaxial tension, Mater. Sci. Eng., A 911 (2024) 146915. https://doi.org/10.1016/j.msea.2024.146915.

[51] Li H, Jin F, Zhang M, Ding J, Bian T, Li J, et al., Decoupling electroplasticity by temporal coordination design of pulse current loading and straining, Mater. Sci. Eng., A 881 (2023) 145435. https://doi.org/10.1016/j.msea.2023.145435.

[52] Lian X-T, An J-L, Wang L, Dong H, A New Strategy for Restraining Dynamic Strain Aging in GH4169 Alloy During Tensile Deformation at High Temperature, Acta Metallurgica Sinica (English Letters) 35 (2022) 1895-1902. https://doi.org/10.1007/s40195-022-01398-3.

[53] Zhou C, Zhan L, Liu C, Huang M, Insights into electron wind force by a helical dislocation reconfiguration, iScience 26 (2023) 106870. https://doi.org/10.1016/j.isci.2023.106870.

[54] Li Y, Wang L, Ran G, Yuan Y, Wu L, Liu X, et al., In-situ TEM investigation of 30 keV he+ irradiated tungsten: Effects of temperature, fluence, and sample thickness on dislocation loop evolution, Acta Mater. 206 (2021) 116618. https://doi.org/10.1016/j.actamat.2020.116618.

[55] Li Y, Ran G, Guo Y, Sun Z, Liu X, Li Y, et al., The evolution of dislocation loop and its interaction with pre-existing dislocation in He+-irradiated molybdenum: in-situ TEM observation and molecular dynamics simulation, Acta Mater. 201 (2020) 462-476. https://doi.org/10.1016/j.actamat.2020.10.022.

[56] Long C, Deutsch MJ, Angelo J, Culbreath C, Yokoyama H, Selinger JV, et al., Frank-Read Mechanism in Nematic Liquid Crystals, Physical Review X 14 (2024) 011044. https://doi.org/10.1103/PhysRevX.14.011044.

[57] Varillas J, Očenášek J, Torner J, Alcalá J, Understanding imprint formation, plastic instabilities and hardness evolutions in FCC, BCC and HCP metal surfaces, Acta Mater. 217 (2021) 117122. https://doi.org/10.1016/j.actamat.2021.117122.

[58] Li Q, Wu M, Xue L, Huang J, Hu Z, Xu G, et al., Controlling CuCrZr alloy properties and microstructure rapidly by pulsed electric treatment (PET), J.

Mater. Sci. 59 (2024) 4680-4699. https://doi.org/10.1007/s10853-024-09516-5.

[59] Zhao J, Ren Z, Zhang H, Wang G-X, Dong Y, Ye C, Electroplasticity in AZ31B subjected to short-duration high-frequency pulsed current, J. Appl. Phys. 125 (2019) 185104. https://doi.org/10.1063/1.5087465.

[60] Guan L, Tang G, Jiang Y, Chu PK, Texture evolution in cold-rolled AZ31 magnesium alloy during electropulsing treatment, J. Alloys Compd. 487 (2009) 309-313. https://doi.org/10.1016/j.jallcom.2009.07.114.

[61] Su J, Ji X, Liu J, Teng J, Jiang F, Fu D, et al., Revealing the decomposition mechanisms of dislocations and metastable α' phase and their effects on mechanical properties in a Ti-6Al-4V alloy, J. Mater. Sci. Technol. 107 (2022) 136-148. https://doi.org/10.1016/j.jmst.2021.07.048.

[62] Kusama T, Omori T, Saito T, Kise S, Tanaka T, Araki Y, et al., Ultra-large single crystals by abnormal grain growth, Nat. Commun. 8 (2017) 354. https://doi.org/10.1038/s41467-017-00383-0.

[63] Homer ER, Johnson OK, Britton D, Patterson JE, Sevy ET, Thompson GB, A classical equation that accounts for observations of non-Arrhenius and cryogenic grain boundary migration, npj Computational Materials 8 (2022) 157. https://doi.org/10.1038/s41524-022-00835-2.

[64] Cantwell PR, Holm EA, Harmer MP, Hoffmann MJ, Anti-thermal behavior of materials, Scr. Mater. 103 (2015) 1-5. https://doi.org/10.1016/j.scriptamat.2015.02.011.

[65] Liu Q, Xiong Z, Liu X, Fang L, Lv C, Yang J, et al., Grain size dependence of grain rotation under high pressure and high temperature, J. Appl. Phys. 134 (2023). https://doi.org/10.1063/5.0164783.

[66] Harris KE, Singh VV, King AH, Grain rotation in thin films of gold, Acta Mater. 46 (1998) 2623-2633. https://doi.org/10.1016/S1359-6454(97)00467-9.

[67] Haslam AJ, Phillpot SR, Wolf D, Moldovan D, Gleiter HJMS, Microstructure EA-sMP, et al., Mechanisms of grain growth in nanocrystalline fcc metals by molecular-dynamics simulation, 318 (2001) 293-312. https://doi.org/10.1016/S0921-5093(01)01266-7.

[68] Waryoba D, Islam Z, Wang B, Haque A, Low temperature annealing of metals with electrical wind force effects, J. Mater. Sci. Technol. 35 (2019) 465-472. https://doi.org/10.1016/j.jmst.2018.09.069.

[69] Zhang G, Li C, Li F, Yu G, Chen C, Pulse current assisted solid granules medium forming of nanocrystalline Ni foil, International Journal of Material Forming 15 (2022) 58. https://doi.org/10.1007/s12289-022-01706-3.

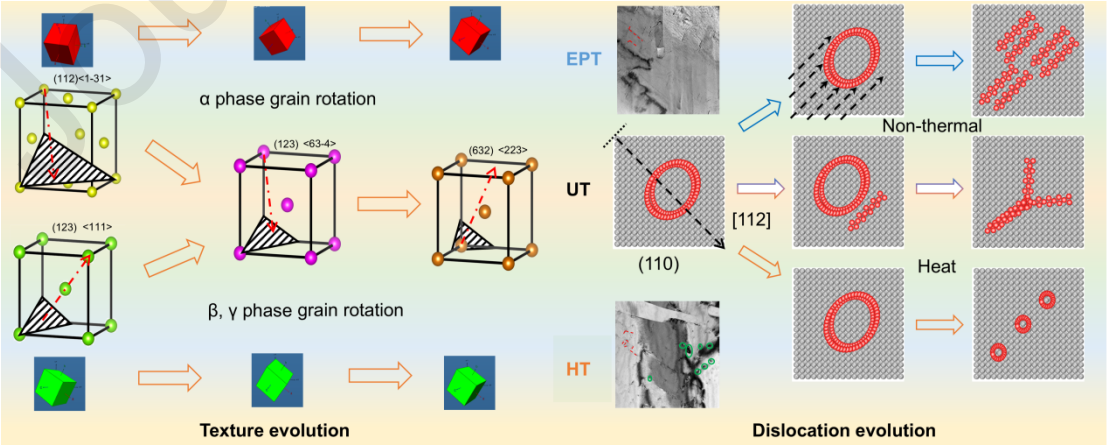

# Highlights

- ✧ Electric pulses sample achieved 69.89% higher elongation without strength loss
- ✧ Electric pulses promote the formation of strong texture parallel to current direction
- ✧ Non-thermal effect promotes the evolution of dislocations to form parallel pairs
- ✧ Texture changes are attributed to grain boundary migration and grain rotation